ADVANCED MATERIALS
www.advmat.de

Mixed Lead Halide Passivation of Quantum Dots

*James Z. Fan, Nigel T. Andersen, Margherita Biondi, Petar Todorović, Bin Sun, Olivier Ouellette, Jehad Abed, Laxmi K. Sagar, Min-Jae Choi, Sjoerd Hoogland, F. Pelayo García de Arquer, and Edward H. Sargent**

Infrared-absorbing colloidal quantum dots (IR CQDs) are materials of interest in tandem solar cells to augment perovskite and cSi photovoltaics (PV). Today's best IR CQD solar cells rely on the use of passivation strategies based on lead iodide; however, these fail to passivate the entire surface of IR CQDs. Lead chloride passivated CQDs show improved passivation, but worse charge transport. Lead bromide passivated CQDs have higher charge mobilities, but worse passivation. Here a mixed lead-halide (MPbX) ligand exchange is introduced that enables thorough surface passivation without compromising transport. MPbX–PbS CQDs exhibit properties that exceed the best features of single lead-halide PbS CQDs: they show improved passivation (43 ± 5 meV vs 44 ± 4 meV in Stokes shift) together with higher charge transport ($4 \times 10^{-2} \pm 3 \times 10^{-3}$ cm^2 V^{-1} s^{-1} vs $3 \times 10^{-2} \pm 3 \times 10^{-3}$ cm^2 V^{-1} s^{-1} in mobility). This translates into PV devices having a record IR open-circuit voltage (IR V_{oc}) of 0.46 ± 0.01 V while simultaneously having an external quantum efficiency of 81 ± 1%. They provide a 1.7× improvement in the power conversion efficiency of IR photons (>1.1 µm) relative to the single lead-halide controls reported herein.

Colloidal quantum dots (CQDs) are a class of solution-processed semiconductor materials of interest for thin-film optoelectronic devices in view of their widely tunable bandgap, a feature that enables application in imaging, communications, displays, and solar energy harvesting.[1–5] CQDs such as metal chalcogenides can be tuned to absorb short-wavelength infrared (IR) (defined as >1 µm) photons—a feature that distinguishes them from semiconducting polymers and metal halide perovskites. This can be exploited to design solar cells that complement the performance of established photovoltaic technologies based on crystalline silicon (cSi) (**Figure 1**a), since silicon fails to absorb IR photons beyond 1100 nm.[6–12]

Single-step solution-processed (i.e., ink-based) IR-PbS QD solar cells have more than doubled in performance in the last decade, and solid-state-exchanged solar cells have reached short-circuit current densities that now exceed 37 mA cm^{-2} for the full spectrum, and over 5 mA cm^{-2} beyond the band edge of crystalline silicon (1100 nm).[7,13,14] PbS IR solar cells have also been reported to harvest the solar spectrum up to 2000 nm, deeper in the infrared than achieved using crystalline germanium solar cells.[15,16] IR solar cells based on PbSe and HgTe CQDs can also harvest light beyond 1100 nm, but their efficiency has, to date, been lower than that of PbS-based devices, principally a result of lower open-circuit voltages.[16,17]

Present-day IR CQD solar cells still have considerable room to improve in efficiency relative to their theoretical potential. Part of suboptimal performance is traced to limited understanding of the surface chemistry of IR CQDs.[8,18] IR CQDs are larger in diameter (4–6 nm) than the wider-bandgap CQDs (E_g = 1.2–1.4 eV) used in full-spectrum harvesting solar cells (≈3 nm). IR CQDs have fewer Pb (111) facets and more charge-neutral PbS (100) planes.[19] Pb (100) surfaces are prone to surface trap formation caused by irreversible oxidation and CQD fusion, and this lowers overall solar cell performance.[9,12,19]

Previous approaches to improve the performance of IR solar cells have relied on various strategies. Device architecture engineering has been pursued by manipulating electron and hole transport layers to improve band alignment with the IR CQD solid and extend charge collection.[11,20,21] Optical engineering has been performed to further enhance light absorption in the CQD solid.[22,23] Finally, different ligand exchange strategies seeking to address the different facet arrangement of larger CQDs have been explored.[6–10,12,14,24] A summary of all currently published IR-PV solar cells is listed (Table S1, Supporting Information).

Ligand-exchange reactions for CQDs seek to passivate their surface states while also permitting electronic coupling among CQDs in the final solid (Figure 1b). In IR-CQD processing, new ligand-exchange strategies have focused on the replacement of long alkane oleic acid molecules using small inorganic anions comprising metal iodide shells.

Successful ligand exchange strategies designed for wider-bandgap CQDs have failed to translate into the larger-diameter CQD regime. This is in part due to the increased presence of

J. Z. Fan, N. T. Andersen, M. Biondi, P. Todorović, Dr. B. Sun, Dr. O. Ouellette, J. Abed, Dr. L. K. Sagar, Dr. M.-J. Choi, Dr. S. Hoogland, Dr. F. P. García de Arquer, Prof. E. H. Sargent
Department of Electrical and Computer Engineering
University of Toronto
10 King's College Road, Toronto, Ontario M5S 3G4, Canada
E-mail: ted.sargent@utoronto.ca

The ORCID identification number(s) for the author(s) of this article can be found under https://doi.org/10.1002/adma.201904304.

DOI: 10.1002/adma.201904304

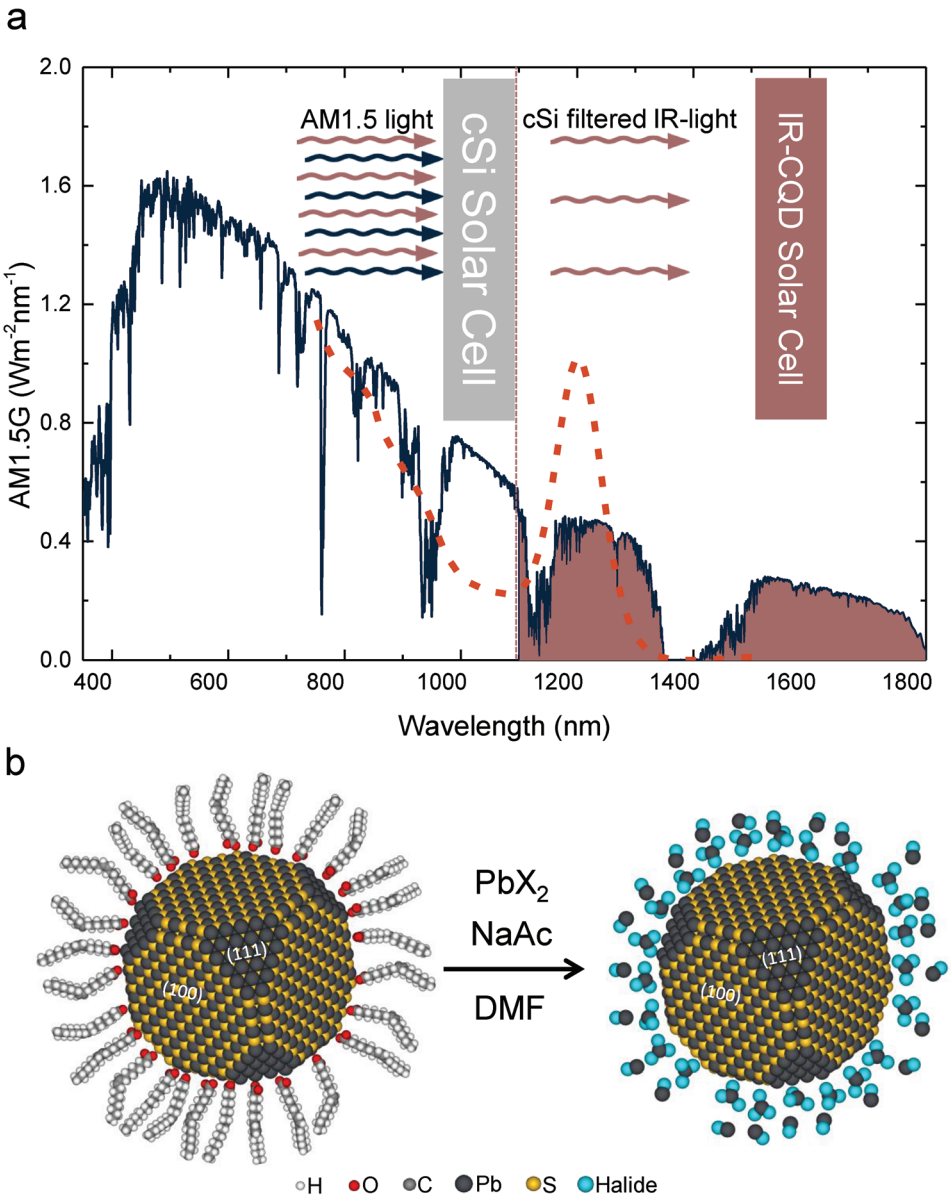

Figure 1. IR PV solar cells. The AM1.5G spectrum is shown with the black curve. The band edge of a cSi solar cell is shown by the dashed line at 1100 nm. a) The shaded area of the AM1.5 reveals additional IR current that can be absorbed with an IR-CQD solar cell. b) Typical lead halide exchange from an oleate capped PbS CQD to a halide-capped PbS CQD.

Pb (100) facets in IR CQDs which—since they are not passivated using the iodide species—leads to CQD fusion and low open-circuit voltages.[6,11,12,25] Using a pure chloride or bromide exchange improves passivation, but compromises charge transport.

Here we report a mixed metal halide passivation strategy that combines multiple lead halides {PbI_2, $PbBr_2$, and $PbCl_2$} to achieve an increased surface metal halide packing. This, as we show, improves passivation and facilitates charge transport. Mixed lead halide PbS (MPbX–PbS) solids exhibit 1.7× higher surface coverage yields, 20% decrease in film Stokes shifts to 42 ± 3 meV, and 1.6× improved mobilities to $4.0 \times 10^{-2} \pm 5 \times 10^{-3}$ cm^2 V^{-1} s^{-1} compared to PbI_2–PbS films. In addition, MPbX–PbS devices exhibit simultaneous improvements in PV parameters over the best features from single lead halide devices, such as enhanced IR open-circuit voltages (V_{oc}) (0.46 ± 0.01 vs 0.44 ± 0.01 V for $PbCl_2$–PbS) and IR short-circuit current densities (J_{sc}) (4.4 ± 0.02 vs 3.7 ± 0.02 mA cm^{-2} for $PbBr_2$–PbS). This leads to a (1.7 ± 0.2)× increase in IR power conversion efficiency (IR PCE) (i.e., PCE for AM1.5G filtered light through a silicon wafer, so the component of AM1.5G that lies >1100 nm) to 6.0 ± 0.2%. This results in the potential of adding 1.17 ± 0.03% extra power points atop those provided by a cSi solar cell.

Recent Ab Initio calculation studies showed that smaller halides such as bromide and chloride have higher binding energies on the Pb (100) facets compared to iodide in PbSe CQDs.[26] Studies have reported that the addition of $PbBr_2$ and

$PbCl_2$ improved the colloidal stability of PbSe CQDs by passivating the PbSe (100) surface with lead halide adlayers.[27] Since PbS and PbSe CQDs share similar surface chemistry, we reasoned that a $PbBr_2$ or $PbCl_2$ solution exchange could potentially improve the passivation of IR-CQDs.[27,28] In one recent investigation, small-angle X-ray scattering studies revealed the presence of a $PbCl_2$ adlayer terminating the Pb (100) surface from a $PbCl_2$-derived PbS synthesis.[29] In addition, a density functional theory study also suggested that the $PbBr_2$ end from a $CsPbBr_3$ perovskite can passivate a PbS (100) slab.[30] These studies hint that the role of both $PbCl_2$ and $PbBr_2$ is used for passviating the Pb (100) surface.

To date, solution-exchanged pure $PbBr_2$ and $PbCl_2$ IR-PbS CQDs have not been studied in experiment as extensively as have been the lead-iodide-based IR-PbS CQDs.

We investigated the colloidal material properties of IR CQD solutions and films made by capping dots with each class of lead halide. Other lead sources from monohalide salts are not explored in this study. $PbBr_2$- and $PbCl_2$-passivated IR-PbS CQDs lead to limited stability in *N*,*N*,-dimethylformamide (DMF) compared to PbI_2–PbS CQDs (Figure S1, Supporting Information), but well-defined photoluminescence (PL) peaks are still present. We posited that CQD aggregation could be the result of the high ionic strength of the DMF solution, and could also be aggravated by partial dissolution of octane in DMF due to the co-solubility of oleic acid in each phase. High lead salt concentrations shrink the electrical double layer around the QDs, thus destabilizing the colloid, and lead halide–capped QDs exhibit poor solubility in nonpolar solvents such as octane.[31,32] The exchanged IR-CQDs can still be redispersed in the DMF–butylamine (DMF–BA) ink, enabling the fabrication of thick, uniform films.[9–11]

Absorbance and PL measurements show that these lead halide PbS CQDs retain their excitonic features in both the ink and final solid state (**Figure 2**a,b). In the CQD ink phase, the PbI_2–PbS shows the highest PL peak, followed by $PbBr_2$–PbS, and $PbCl_2$–PbS. The high PL peak is indicative of the colloidal stability in the ink; the formation of a thicker electrical double layer will space the dots apart, improving radiative recombination, hence increasing the PL intensity (Figure 2a).[33,34] However, this trend changed when we studied the corresponding films. The $PbCl_2$–PbS film showed the highest PL peak, followed by PbI_2–PbS and $PbBr_2$–PbS (Figure 2b). A high PL peak for a CQD film suggests improved passivation due to a thicker ligand shell. The thicker shell improves confinement, hence increasing the PL intensity, but raises the prospect of worsened charge transport.[35,36]

We therefore fabricated field-effect transistors (FETs) to characterize the mobilities of the single lead halide films (Figure S2 and Table S2, Supporting Information). $PbBr_2$–PbS CQDs exhibited the highest mobility ($2.8 \times 10^{-2} \pm 3 \times 10^{-3}$ cm^2 V^{-1} s^{-1}), followed by PbI_2–PbS ($2.5 \times 10^{-2} \pm 3 \times 10^{-3}$ cm^2 V^{-1} s^{-1}), and $PbCl_2$–PbS ($1 \times 10^{-5} \pm 5 \times 10^{-6}$ cm^2 V^{-1} s^{-1}). This explains in part the film PL findings; high mobilities result in faster nonradiative recombination, such as trap-assisted recombination, thereby reducing the fraction of radiative recombination (Figure 2c).[37]

The Stokes shift and PL full width at half maximum (FWHM) for each lead halide species also change following film formation (Figure 2d,e; Tables S3 and S4, Supporting Information). A smaller Stokes shift in the solid phase implies that the energetic disorder of the CQD is minimized due to reduced CQD aggregation, leading to improvements in V_{oc}.[12,38,39] Likewise, a narrower PL FWHM suggests a more monodispersed CQD ensemble.[40] The Stokes shift and PL FWHM for the PbI_2–PbS increased the most between the ink and solid state phases. This suggests that some CQDs may have fused during the film formation process, increasing the polydispersity of the film (Figure 2c,d). Since PbI_2 is mostly responsible for passivating the Pb (111) surface, we reasoned that a large fraction of CQDs may fuse through the Pb (100) facet.[19] This will be detrimental to PV performance since charge carriers will funnel to the fused bandtail CQDs.[41] These polydisperse fused-bandtail CQDs have smaller bandgaps that behave as deep traps that hinder transport.[8,41] Conversely, the decrease in Stokes shift and PL FWHM for the $PbCl_2$–PbS CQDs complements the improved passivation. Finally, the slight decrease in Stokes shift and slight increase in PL FWHM for the $PbBr_2$–PbS CQDs suggest that the passivation properties are mostly preserved for this species.

Taking the above studies as a whole, we summarize carrier transport in (Figure 2f–h): the low bandgap of PbI_2 improves the mobility of this PbS solid, but smaller bandgap-fused dots may act as an electron acceptor; $PbCl_2$–PbS films may have the best passivation, but the adlayers hinder the transport of the system; and the $PbBr_2$–PbS films have slightly worse passivation than the $PbCl_2$–PbS, but do not suffer from a high degree of dot fusion.

Maximizing the PCE of IR-PV requires both excellent transport and passivation. We sought to terminate the CQDs using a mixture of lead halides in order to reach a lead halide shell equilibrium that closely packs each dot without fusion. It was previously reported that lead halides self-ionize in polar solvents into anionic $[PbX_{n+1}]^-$ and cationic $[PbX_{n-1}]^+$ species.[42,43] Mixing the three lead halides into one precursor solution is expected therefore to allow each $[PbX_{n+1}]^-$ species to exchange with oleate ligands on a given CQD facet. Large lead iodide ligands would passivate lead-rich Pb (111) surfaces and provide good charge transport,[44] while smaller lead halides would passivate Pb (100) surfaces to reduce surface defects and CQD fusion. We term this the mixed lead halide ligand exchange strategy for lead sulfide quantum dots (MPbX–PbS). Transmission electron microscopy (TEM) reveals the shape of the MPbX–PbS QDs (Figure S3, Supporting Information). IR CQDs are dominated by charge-neutral PbS (100) and PbS (110) rather the lead-rich Pb (111) planes, as seen in previous reports.[45] The lighter contrast on the edge of the QD suggests a mixed lead halide shell, while a zoomed out image hints at its role in preventing IR-CQDs from fusing.

We pursued therefore the addition of a lower amount of each single lead halide (e.g., $<2 \times 10^{-3}$ M halides/mg CQD) for selective passivation without the formation of thick adlayers. We explored different combinations of lead halide mixtures and reached a maximum lead halide content of 4.7×10^{-3} M mg^{-1} of IR CQDs (Tables S5 and S6, Supporting Information). Single lead halide ligand exchanges (i.e., PbI_2–, $PbBr_2$–, or $PbCl_2$–PbS) at 4.7×10^{-3} M mg^{-1} of CQDs were also used to fabricate IR CQDs and studied alongside the MPbX–PbS CQDs.

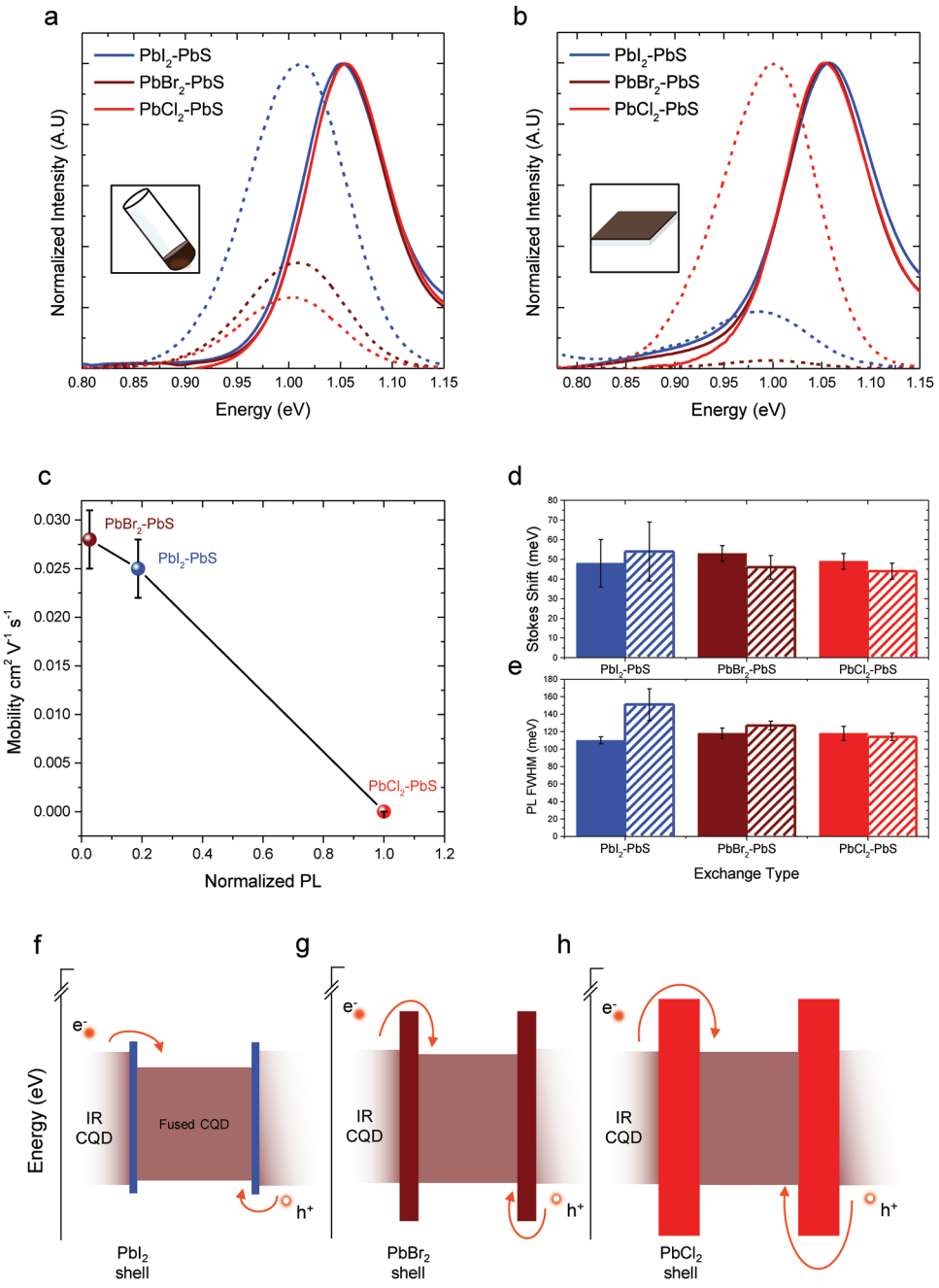

Figure 2. Materials' characterization for single lead halide (PbI_2, $PbBr_2$, and $PbCl_2$)–passivated IR PbS CQDs (blue, brown, and red). a,b) Normalized photoluminescence (dotted lines) to absorbance (solid lines) spectra are shown for halide-passivated PbS in the ink (a) and film (b). c) Film mobility versus normalized photoluminescence height. d) Changes in Stokes shift from the ink (solid) to film (dashed) phase. e) Changes in the photoluminescence full width half maximum (FWHM) from the ink (solid) to film (dashed) phase. f–h) Schematic of carrier transport in each CQD solid for PbI_2–PbS (f), $PbBr_2$–PbS (g), and $PbCl_2$–PbS (h).

X-ray photoelectron spectroscopy (XPS) was used to study the behavior of surface lead halides on each IR PbS CQD. XPS spectra (i.e., I 3d, Br 3d, and Cl 2p) showed that each individual halide is present in their respective PbS films, while the MPbX–PbS film had all three (**Figure 3**a–c). We reference data to the native sulfur 2s peak at 161.3 eV to study the relative concentration of each surface lead halide, since no additional sulfur sources were added to the ligand-exchange solution (Table S6, Supporting Information). The surface coverage yields—calculated as the ratio of halide:sulfur divided by the added lead halide precursor ($\times 10^{-3}$ M mg^{-1})—show the effectiveness of halide passivation for different treatments (Figure 3e,f). Iodide has the lowest surface coverage yield, followed by bromide, and then chloride for the single lead halide IR dots. The larger fraction of Pb (100) surfaces existing on the surface of IR CQDs prevent the full passivation

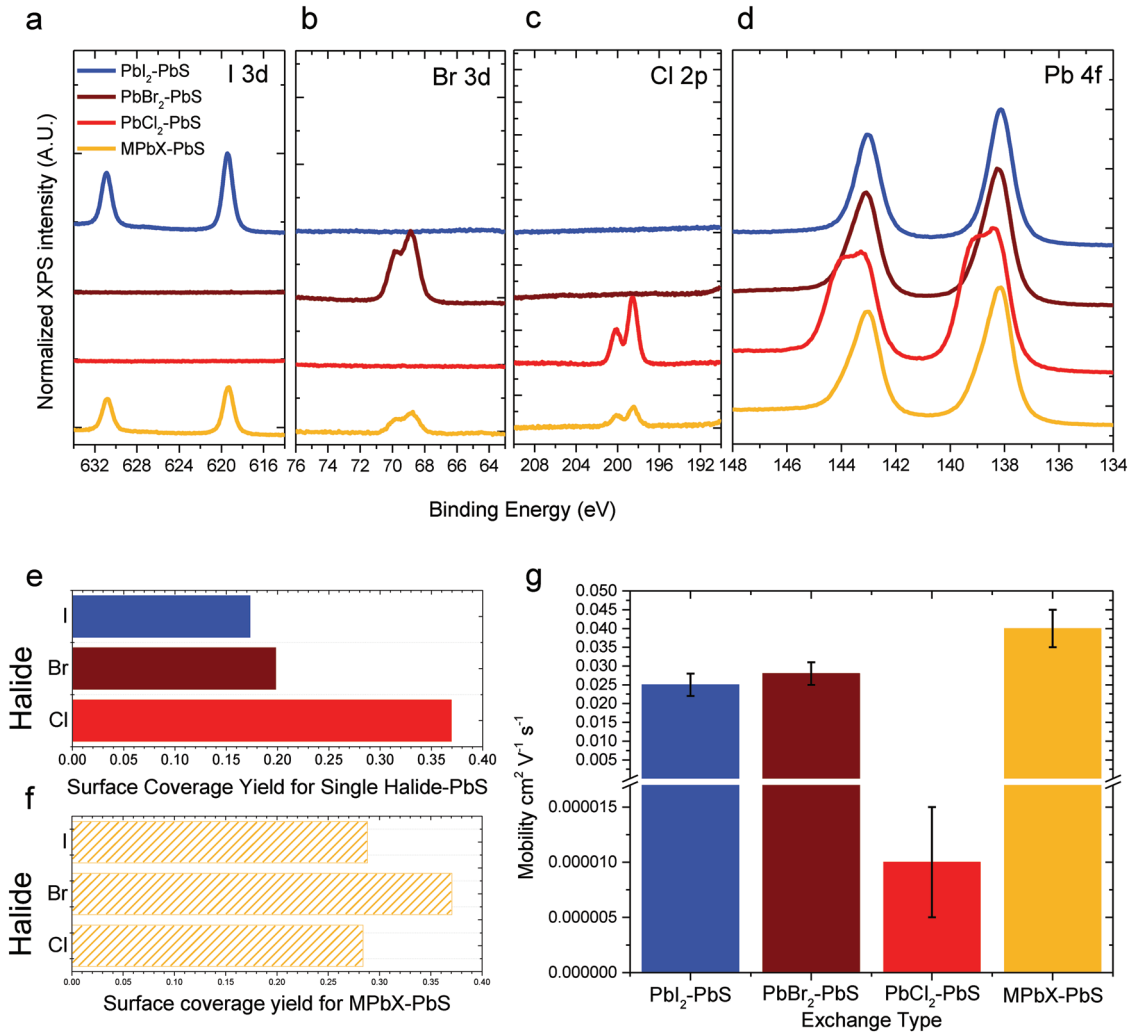

Figure 3. Materials' characterization comparing all lead halide–passivated PbS films (blue: PbI_2, brown: $PbBr_2$, red: $PbCl_2$, and gold: MPbX). a–d) X-ray photoelectron (XPS) of the I 3d, Br 3d, Cl 2p, and Pb 4f of all halide-passivated films. e,f) XPS surface coverage yields for single halide PbS films (e) and MPbX–PbS films (f). g) Mobility of each halide-passivated PbS solid.

of the dot through a pure iodide exchange.[12] The surface coverage yield for the pure bromide dot slightly increases due to the shorter Pb—Br bond, allowing closer packing of the lead halides on the surface of the dot.[46,47] Finally, using the pure chloride exchange resulted in the highest surface coverage yield because of its short Pb—Cl bond distance and the ability to passivate Pb (100) surfaces.[48,49] We observe the growth of thick $PbCl_2$ shells on dots, evidenced by the extra 139 eV peak appearing in the Pb 4f 7/2 spectrum, which may act as an insulator by spacing the $PbCl_2$–PbS CQDs further part, leading to worsened charge transport (Figure 3d; Figure S4 and Table S7, Supporting Information). Thinner lead halide shells evidenced by lower XPS halide:sulfur ratios provide an explanation for higher mobilities in PbI_2–PbS and $PbBr_2$–PbS films. When comparing to the single-halide CQDs, the MPbX–PbS CQDs had higher surface coverage yields for iodide and bromide by 1.7× and 1.9×, respectively, but a decreased value for chloride by 0.8× due to the absence of thick $PbCl_2$ shells.

To assess the impact of the surface lead halide arrangement on passivation and charge transport, we carried out optical and electrical spectroscopies. Absorbance and PL studies for MPbX–PbS reveal that it has the highest PL in the ink phase, while having low PL in the film phase (Figure S5, Supporting Information)—this suggests good QD coupling and high charge mobility.[35] MPbX–PbS CQDs show the lowest Stokes shift (47 ± 4 and 43 ± 5 meV for ink and film, respectively) and the narrowest PL FWHM (103 ± 3 and 109 ± 4 meV for ink and film, respectively), indicating excellent CQD monodispersity in both phases (Tables S8 and S9, Supporting Information). These findings are confirmed with FET studies, which show that MPbX–PbS films have the highest mobility ($4.0 \times 10^{-2} \pm 5 \times 10^{-3}$ cm^2 V^{-1} s^{-1}) of all lead halide surface configurations (Table S2, Supporting Information). The low amounts of each single lead halide used in the exchange allow all species to achieve a lead halide equilibrated shell, thus giving a significant improvement in passivation while favoring transport. As an example, MPbX–PbS solids exhibit an

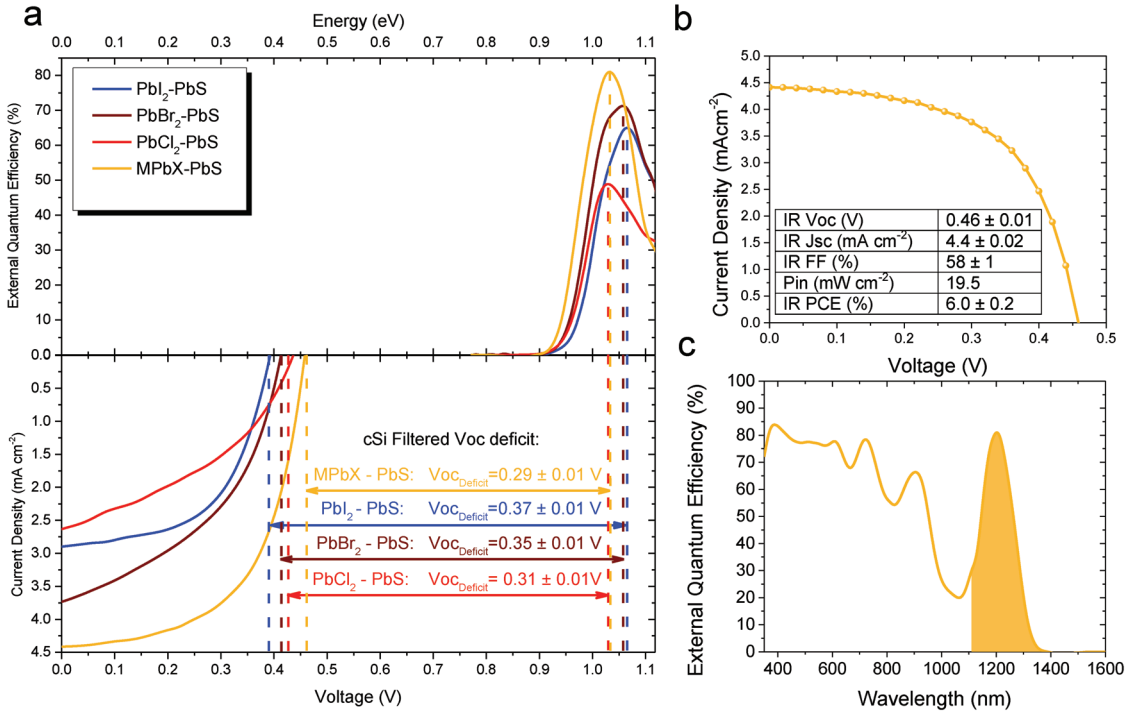

Figure 4. Device analysis and champion device performance. a, top) The external quantum efficiency of IR-CQD devices showing the region absorbed after a crystalline silicon filter. IR-filtered *J–V* sweeps of each PbS device. a, bottom)The V_{oc} deficit is also calculated. b) The cSi-filtered *J–V* sweep for the champion MPbX–PbS device. The corresponding external quantum efficiency (EQE) measurement for the champion MPbX–PbS device. c) The shaded area represents the si-filtered IR current.

≈10 meV decrease in films Stokes shift, ≈1.7× higher surface halide coverage yield, and ≈1.6× improved mobility over a pure PbI_2-passivated CQD.

We then sought to take advantage of these properties and implemented IR CQD solar cells based on MPbX–PbS. We used the architecture of indium-doped tin oxide (ITO)/zinc oxide (ZnO)/lead halide–PbS/1,2,-ethanedithiol (EDT)–PbS/Au (Figure S6, Supporting Information).[41,50,51] The infrared harvesting portion (>1100 nm, <1.13 eV) of each external quantum efficiency (EQE) spectrum and their corresponding cSi-filtered *J–V* curves are presented in the same figure (**Figure 4**a). Since the solar intensity is lower through a simulated silicon filter, the IR devices tested through the 1100 nm long-pass filter exhibit higher fill factors due to lower resistive losses incurred at lower current densities.[52] All reported J_{sc} values are obtained from multiplying the integrated EQE spectra from the AM1.5G spectrum, due to the spectral mismatch between the solar simulator and actual AM1.5G spectrum.[53,54] We present also the calculated IR-V_{oc} deficit for the various devices.[55] The MPbX–PbS device has the lowest IR-V_{oc} deficit, followed by $PbCl_2$–PbS, $PbBr_2$–PbS, and finally PbI_2–PbS (Tables S9 and S11, Supporting Information). A lower IR-V_{oc} deficit suggests that the mixed lead halide exchange improves the passivation of IR CQDs. In addition, the lower IR-V_{oc} deficit can be explained by considering the film Stokes shift versus the IR-V_{oc} (Figure S7, Supporting Information).[38,39] The MPbX–PbS devices show the lowest Stokes shift, followed by $PbCl_2$–PbS, $PbBr_2$–PbS, and PbI_2–PbS; the trend agrees with the increasing V_{oc} deficit. This is explained by the studies of mobility and passivation since the MPbX–PbS films showed the best results for both. We also observe that the enhancement of the EQE exciton peak is higher for the MPbX–PbS device. This may arise from a favorable resonant absorption for its optimized active layer thickness.[56] To gain further insight, we carried out internal quantum efficiency (IQE) measurements for another set of representative devices to study the efficiency of photon collection in the infrared region (Figure S8 and Tables S12 and S13, Supporting Information). PbI_2–PbS devices start with a high value of over 90% in the blue wavelength region, but drop to 80% in the infrared region, indicating worse conversion of infrared photons into carriers for an IR solar cell. The $PbBr_2$–PbS and $PbCl_2$–PbS devices maintain a flat curve of around 85% across the solar spectrum. MPbX–PbS maintains an IQE of ≈90% across the entire solar spectrum, indicating that this device collects photocarriers associated with both short- and long-wavelength photoexcitation. Dark current measurements reveal that the MPbX–PbS devices have the lowest reverse saturation current out of the set, indicative of a higher quality device. Champion MPbX–PbS devices achieve an IR-V_{oc} of 0.46 ± 0.01 V while reaching an external quantum efficiency of 81 ± 1% in the infrared region, giving an IR-J_{sc} value of 4.4 ± 0.02 mA cm^{-2}. This is the highest IR-V_{oc} reported to date.[6–12,14,21,23,56] This results in an IR-PbS solar cell capable of having an uncertified IR-PCE of 6.0 ± 0.2%, which translates to adding 1.17 ± 0.03% power points to an existing cSi solar cell in a four-terminal tandem configuration (Figure 4b,c).

In summary, we present a new mixed lead halide ligand-exchange strategy that simultaneously provides efficient

passivation and IR CQD coupling. Previous single lead halide passivation strategies had resulted in underperforming IR solar cells due to either poor passivation or transport. The MPbX–PbS exchange allows each lead halide to exchange onto their most energetically favored IR-PbS facet, resulting in both improvements in passivation and transport. These devices show higher IR open-circuit voltages and maintain high short-circuit current densities. This work provides new insights into the understanding of IR PbS CQDs, and will benefit the broader optoelectronic community for those working on IR photodetectors or IR light-emitting diodes.

Experimental Section

All experiments and methods are described in detail in the Supporting Information.

Supporting Information

Supporting Information is available from the Wiley Online Library or from the author.

Acknowledgements

J.Z.F., N.T.A., and M.B. contributed equally to this work. The authors thank A. Seifitokaldani L. Levina, E. Palmiano, R. Wolowiec, and D. Kopilovic for their help during the course of the study. This research was funded by the Natural Sciences and Engineering Research Council of Canada (NSERC), Alexander Graham Bell Canada Graduate Scholarships (CGS-D), Materials for Enhanced Energy Technologies (MEET) scholarships, and the NSERC Collaborative Research and Training Experience (CREATE) Program (Grant No. 466083).

Conflict of Interest

The authors declare no conflict of interest.

Keywords

infrared photovoltaics, ligand exchange, nanomaterials, quantum dots

Received: July 5, 2019
Revised: September 24, 2019
Published online:

[1] F. W. Wise, *Acc. Chem. Res.* **2000**, *33*, 773.
[2] N. Huo, S. Gupta, G. Konstantatos, *Adv. Mater.* **2017**, *29*, 1606576.
[3] M. C. Weidman, Q. Nguyen, D. M. Smilgies, W. A. Tisdale, *Chem. Mater.* **2018**, *30*, 807.
[4] Y. Jiang, S. Y. Cho, M. Shim, *J. Mater. Chem. C* **2018**, *6*, 2618.
[5] T. Kawawaki, H. Wang, T. Kubo, K. Saito, J. Nakazaki, H. Segawa, T. Tatsuma, *ACS Nano* **2015**, *9*, 4165.
[6] Y. Bi, S. Pradhan, S. Gupta, M. Z. Akgul, A. Stavrinadis, G. Konstantatos, *Adv. Mater.* **2018**, *30*, 1704928.
[7] A. Kiani, B. R. Sutherland, Y. Kim, O. Ouellette, L. Levina, G. Walters, T. Dinh, M. Liu, O. Voznyy, X. Lan, A. J. Labelle, A. H. Ip, A. Proppe, G. H. Ahmed, O. F. Mohammed, S. Hoogland, E. H. Sargent, *Appl. Phys. Lett.* **2016**, *109*, 183105.
[8] A. H. Ip, A. Kiani, I. J. Kramer, O. Voznyy, H. F. Movahed, L. Levina, M. M. Adachi, S. Hoogland, E. H. Sargent, *ACS Nano* **2015**, *9*, 8833.
[9] J. Z. Fan, M. Liu, O. Voznyy, B. Sun, L. Levina, R. Quintero-Bermudez, M. Liu, O. Ouellette, F. P. García de Arquer, S. Hoogland, E. H. Sargent, *ACS Appl. Mater. Interfaces* **2017**, *9*, 37536.
[10] J. W. Jo, J. Choi, F. P. García De Arquer, A. Seifitokaldani, B. Sun, Y. Kim, H. Ahn, J. Fan, R. Quintero-Bermudez, J. Kim, M. J. Choi, S. W. Baek, A. H. Proppe, G. Walters, D. H. Nam, S. Kelley, S. Hoogland, O. Voznyy, E. H. Sargent, *Nano Lett.* **2018**, *18*, 4417.
[11] J. Choi, J. W. Jo, F. P. G. de Arquer, Y. B. Zhao, B. Sun, J. Kim, M. J. Choi, S. W. Baek, A. H. Proppe, A. Seifitokaldani, D. H. Nam, P. Li, O. Ouellette, Y. Kim, O. Voznyy, S. Hoogland, S. O. Kelley, Z. H. Lu, E. H. Sargent, *Adv. Mater.* **2018**, *30*, 1801720.
[12] Y. Kim, F. Che, J. W. Jo, J. Choi, F. P. García de Arquer, O. Voznyy, B. Sun, J. Kim, M.-J. Choi, R. Quintero-Bermudez, F. Fan, C. S. Tan, E. Bladt, G. Walters, A. H. Proppe, C. Zou, H. Yuan, S. Bals, J. Hofkens, M. B. J. Roeffaers, S. Hoogland, E. H. Sargent, *Adv. Mater.* **2019**, *31*, 1805580.
[13] F. Tan, H. Tan, M. I. Saidaminov, M. Wei, M. Liu, A. Mei, P. Li, B. Zhang, C. Tan, X. Gong, Y. Zhao, A. R. Kirmani, Z. Huang, J. Z. Fan, R. Quintero-Bermudez, J. Kim, Y. Zhao, O. Voznyy, Y. Gao, F. Zhang, L. J. Richter, Z.-H. Lu, W. Zhang, E. H. Sargent, *Adv. Mater.* **2019**, *31*, 1807435.
[14] Y. Bi, A. Bertran, S. Gupta, I. Ramiro, S. Pradhan, S. Christodoulou, S. N. Majji, M. Z. Akgul, G. Konstantatos, *Nanoscale* **2019**, *11*, 838.
[15] V. Sorianello, L. Colace, C. Maragliano, D. Fulgoni, L. Nash, G. Assanto, *Opt. Mater. Express* **2013**, *3*, 216.
[16] D. Cui, J. Xu, T. Zhu, G. Paradee, S. Ashok, M. Gerhold, *Appl. Phys. Lett.* **2006**, *88*, 183111.
[17] M. Nam, S. Kim, S. Kim, S. Jeong, S. W. Kim, K. Lee, *Sol. Energy Mater. Sol. Cells* **2014**, *126*, 163.
[18] E. H. Sargent, *Nat. Photonics* **2009**, *3*, 325.
[19] H. Choi, J. Ko, Y. Kim, S. Jeong, *J. Am. Chem. Soc.* **2013**, *135*, 5278.
[20] H. Wang, T. Kubo, J. Nakazaki, H. Segawa, *ACS Energy Lett.* **2017**, *2*, 2110.
[21] J. Kim, O. Ouellette, O. Voznyy, M. Wei, J. Choi, M. J. Choi, J. W. Jo, S. W. Baek, J. Fan, M. I. Saidaminov, B. Sun, P. Li, D. H. Nam, S. Hoogland, Z. H. Lu, F. P. García de Arquer, E. H. Sargent, *Adv. Mater.* **2018**, *30*, 1803830.
[22] O. Ouellette, N. Hossain, B. R. Sutherland, A. Kiani, F. P. García De Arquer, H. Tan, M. Chaker, S. Hoogland, E. H. Sargent, *ACS Energy Lett.* **2016**, *1*, 852.
[23] S. W. Baek, P. Molet, M. J. Choi, M. Biondi, O. Ouellette, J. Fan, S. Hoogland, F. P. G. de Arquer, A. Mihi, E. H. Sargent, *Adv. Mater.* **2019**, *31*, 1901745.
[24] M. Liu, F. Che, B. Sun, O. Voznyy, A. Proppe, R. Munir, M. Wei, R. Quintero-Bermudez, L. Hu, S. Hoogland, A. Mandelis, A. Amassian, S. O. Kelley, F. P. Garciá De Arquer, E. H. Sargent, *ACS Energy Lett.* **2019**, *4*, 1225.
[25] Y. Cao, A. Stavrinadis, T. Lasanta, D. So, G. Konstantatos, *Nat. Energy* **2016**, *1*, 16035.
[26] B. Wang, H. Xia, Z. Zhang, J. Yang, R. Patterson, S. Huang, S. Shrestha, G. Conibeer, *RSC Adv.* **2016**, *6*, 104699.
[27] J. Y. Woo, J. H. Ko, J. H. Song, K. Kim, H. Choi, Y. H. Kim, D. C. Lee, S. Jeong, *J. Am. Chem. Soc.* **2014**, *136*, 8883.
[28] J. Zhang, J. Gao, E. M. Miller, J. M. Luther, M. C. Beard, *ACS Nano* **2014**, *8*, 614.
[29] S. W. Winslow, Y. Liu, J. W. Swan, W. A. Tisdale, *ACS Mater. Lett.* **2019**, *1*, 209.
[30] Y. K. Jung, K. T. Butler, A. Walsh, *J. Phys. Chem. C* **2017**, *121*, 27351.
[31] C. W. Hoerr, H. J. Harwood, *J. Phys. Chem.* **1952**, *56*, 1068.

[32] R. M. Dragoman, M. Grogg, M. I. Bodnarchuk, P. Tiefenboeck, D. Hilvert, D. N. Dirin, M. V. Kovalenko, *Chem. Mater.* **2017**, *29*, 9416.
[33] A. H. Proppe, J. Xu, R. P. Sabatini, J. Z. Fan, B. Sun, S. Hoogland, S. O. Kelley, O. Voznyy, E. H. Sargent, *Nano Lett.* **2018**, *18*, 7052.
[34] Z. Yang, J. Z. Fan, A. H. Proppe, F. P. G. De Arquer, D. Rossouw, O. Voznyy, X. Lan, M. Liu, G. Walters, R. Quintero-Bermudez, B. Sun, S. Hoogland, G. A. Botton, S. O. Kelley, E. H. Sargent, *Nat. Commun.* **2017**, *8*, 1325.
[35] B.-R. Hyun, G. G. Malliaras, F. W. Wise, T. Hanrath, J. J. Choi, L. Sun, D. Stachnik, A. C. Bartnik, *Nat. Nanotechnol.* **2012**, *7*, 369.
[36] X. Li, Y. B. Zhao, F. Fan, L. Levina, M. Liu, R. Quintero-Bermudez, X. Gong, L. N. Quan, J. Fan, Z. Yang, S. Hoogland, O. Voznyy, Z. H. Lu, E. H. Sargent, *Nat. Photonics* **2018**, *12*, 159.
[37] D. Zhitomirsky, O. Voznyy, L. Levina, S. Hoogland, K. W. Kemp, A. H. Ip, S. M. Thon, E. H. Sargent, *Nat. Commun.* **2014**, *5*, 3803.
[38] Y. Liu, D. Kim, O. P. Morris, D. Zhitomirsky, J. C. Grossman, *ACS Nano* **2018**, *12*, 2838.
[39] O. Voznyy, L. Levina, F. Fan, G. Walters, J. Z. Fan, A. Kiani, A. H. Ip, S. M. Thon, A. H. Proppe, M. Liu, E. H. Sargent, *Nano Lett.* **2017**, *17*, 7191.
[40] T. R. Ravindran, A. K. Arora, B. Balamurugan, B. R. Mehta, *Nanostruct. Mater.* **1999**, *11*, 603.
[41] M. Liu, O. Voznyy, R. Sabatini, F. P. G. de Arquer, R. Munir, A. H. Balawi, X. Lan, F. Fan, G. Walters, A. R. Kirmani, S. Hoogland, F. Laquai, A. Amassian, E. H. Sargent, *Nat. Mater.* **2016**, *16*, 258.
[42] D. N. Dirin, S. Dreyfuss, M. I. Bodnarchuk, G. Nedelcu, P. Papagiorgis, G. Itskos, M. V. Kovalenko, *J. Am. Chem. Soc.* **2014**, *136*, 6550.
[43] *Inorganic Chemistry of the Main-Group Elements* (Ed: C. C. Addison), The Royal Society Of Chemistry, London, UK **1977**.
[44] X. Lan, O. Voznyy, F. P. García De Arquer, M. Liu, J. Xu, A. H. Proppe, G. Walters, F. Fan, H. Tan, M. Liu, Z. Yang, S. Hoogland, E. H. Sargent, *Nano Lett.* **2016**, *16*, 4630.
[45] F. Bertolotti, D. N. Dirin, M. Ibáñez, F. Krumeich, R. Frison, O. Voznyy, E. H. Sargent, V. Maksym, A. Guagliardi, N. Masciocchi, *Nat. Mater.* **2016**, *15*, 987.
[46] W. Geng, L. Zhang, Y. N. Zhang, W. M. Lau, L. M. Liu, *J. Phys. Chem. C* **2014**, *118*, 19565.
[47] A. D. Baranyi, M. Onyszchuk, Y. Le Page, G. Donnay, *Can. J. Chem.* **1977**, *55*, 849.
[48] A. J. Elleman, H. Wilman, *Proc. Phys. Soc., London, Sect. A* **1949**, *62*, 344.
[49] I. Hargittai, J. Tremmel, E. Vajda, A. A. Ishchenko, A. A. Ivanov, L. S. Ivashkevich, V. P. Spiridonov, *J. Mol. Struct.* **1977**, *42*, 147.
[50] J. Xu, O. Voznyy, M. Liu, A. R. Kirmani, G. Walters, R. Munir, M. Abdelsamie, A. H. Proppe, A. Sarkar, F. P. García De Arquer, M. Wei, B. Sun, M. Liu, O. Ouellette, R. Quintero-Bermudez, J. Li, J. Fan, L. Quan, P. Todorovic, H. Tan, S. Hoogland, S. O. Kelley, M. Stefik, A. Amassian, E. H. Sargent, *Nat. Nanotechnol.* **2018**, *13*, 456.
[51] C.-H. M. Chuang, P. R. Brown, V. Bulović, M. G. Bawendi, *Nat. Mater.* **2014**, *13*, 796.
[52] M. Wolf, H. Rauschenbach, *Adv. Energy Convers.* **1963**, *3*, 455.
[53] V. Shrotriya, G. Li, Y. Yao, T. Moriarty, K. Emery, Y. Yang, *Adv. Funct. Mater.* **2006**, *16*, 2016.
[54] J. Nelson, *The Physics of Solar Cells*, Imperial College Press, London, UK **2003**.
[55] W. Shockley, H. J. Queisser, *J. Appl. Phys.* **1961**, *32*, 510.
[56] B. Sun, O. Ouellette, F. P. G. de Arquer, O. Voznyy, Y. Kim, M. Wei, A. H. Proppe, M. I. Saidaminov, J. Xu, M. Liu, P. Li, J. Z. Fan, J. W. Jo, H. Tan, F. Tan, S. Hoogland, Z. H. Lu, S. O. Kelley, E. H. Sargent, *Nat. Commun.* **2018**, *9*, 4003.

